

# Driving Towards Highly Selective and Coking-Resistant Natural Gas Reforming Through a Hybrid Oxygen Carrier Design

Lang Qin<sup>+</sup>,<sup>[a]</sup> Yu-Yen Chen<sup>+</sup>,<sup>[a]</sup> Mengqing Guo<sup>+</sup>,<sup>[a]</sup> Yan Liu,<sup>[a]</sup> Jonathan A. Fan,<sup>[b]</sup> and Liang-Shih Fan<sup>\*[a]</sup>

Carbon deposition can be promoted by catalyst-assisted C–H bond dissociation, which is one of the most concerning issues in reaction engineering. Treatment of carbon contamination inevitably generates CO<sub>2</sub> which has a detrimental effect on the environment. Consequently, the development of efficient oxygen carriers is important to commercial viability of chemical looping processes. In this work, density functional theory (DFT) calculations were conducted and reveal that carbon deposition is a cascade reaction of accumulative C–C bond forming that

deactivates LFO surface due to gradual accumulation of lattice oxygen vacancies. Guided by DFT mechanistic predictions, we tailor catalytic reactive perovskite LaFeO<sub>3</sub> (LFO) with high oxygen carrying hematite Fe<sub>2</sub>O<sub>3</sub> (FO) into a hybrid oxygen carrier LFO-FO. The LFO-FO oxygen carrier exhibits excellent carbon inhibition capability and high reactivity with syngas selectivity above 98%. This work proposes a promising strategy toward oxygen carrier development with low cost, high reactivity, and selectivity for chemical looping technology.

## 1. Introduction

Alkanes are potential precursors to a variety of value-added chemicals. Nevertheless, alkanes are relatively inert, exhibiting little or no reactivity at conditions typical for activating functional group reactions in organic compounds due to the lack of low-lying vacant orbitals or lone pair electrons.<sup>[1]</sup> Converting alkanes universally involves catalysts plus high temperature or pressure due to their strongly localized electron pairs. However, catalytic alkane conversions with vigorous bond dissociations would lead to violent surface carbon deposition that deactivates the active sites, which is one of the most concerning issues in reaction engineering. Treatment of carbon contamination inevitably generates CO<sub>2</sub> which has a detrimental effect on the environment. Moreover, such carbon deposition is a cascade reaction that goes beyond control once carbon clusterization is triggered, which significantly hinders commercial processes that directly convert alkanes to valuable chemicals. Hence, processes and catalysts that can efficiently utilize

alkanes while having strong carbon resistance have long been sought in the clean energy industry.

Among all the alkanes, methane is not only the most stable molecule due to its intact structure, but also links to climate change due to its natural and anthropogenic origin. Recently, methane has developed into the fastest growing energy and chemical production resource<sup>[2,3]</sup> due to the widespread reserve availability and booming new production technology. The prominent processes leading to the conversion of methane into hydrogen-rich products have been sought after as viable carbon-neutral or low-carbon energy systems in the prospective energy outlook.<sup>[4]</sup> Syngas is a valuable feedstock for multiple energy intensive industrial chemical processes.<sup>[5]</sup> Hence numerous catalysis and chemical processes have been pursued to transform methane into syngas, notably, steam reforming, carbon dioxide (dry) reforming, and auto-thermal reforming using oxygen with CO<sub>2</sub> or steam (ATR).<sup>[6–12]</sup> In most of these processes, high concentration by-products such as CO<sub>2</sub> and H<sub>2</sub>O are generated due to the inevitably excess usage of air or steam, which reduces the syngas yield and purity with a high energy penalty. Noble metal oxide based catalysts were commonly used in improving the reforming efficiency,<sup>[13]</sup> which unfortunately promotes carbon deposition that not only impedes the activity of oxygen carriers but also creates CO<sub>2</sub> in their regeneration reactions. The same issue arises also in the hydrocarbon reforming processes that employ metal catalysts, in which a low ration of oxygen to carbon that is optimal for the process efficiency results in fatal carbon deposition that deactivates the catalyst. It is therefore imperative to identify processes for methane-to-syngas conversions that are efficient and cost-effective while capable of inhibiting elemental carbon accumulation.

Chemical looping processing of methane (Figure 1) is an attractive and efficient platform for production of syngas and

[a] Dr. L. Qin,<sup>+</sup> Y.-Y. Chen,<sup>+</sup> M. Guo,<sup>+</sup> Y. Liu, Prof. L.-S. Fan  
William G. Lowrie Department of Chemical and Biomolecular Engineering  
The Ohio State University  
151 W. Woodruff Ave  
Columbus, OH 43210 (USA)  
E-mail: fan.1@osu.edu  
qin.96@osu.edu

[b] J. A. Fan  
Department of Electrical Engineering  
Ginzton Laboratory  
Spilker Engineering and Applied Sciences  
Stanford University  
348 Via Pueblo Mall  
Stanford, CA 94305 (USA)

[<sup>+</sup>] These authors contributed equally to this work.

Supporting information for this article is available on the WWW under  
<https://doi.org/10.1002/cctc.202001199>

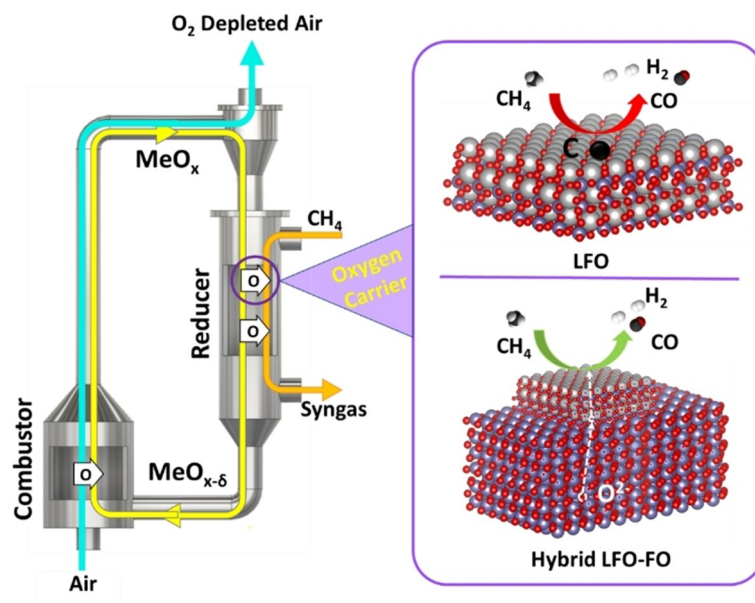


**Figure 1.** Schematic illustration of chemical looping methane partial oxidation using hybrid FO/LFO in comparison with LFO.

value-added chemicals.<sup>[14–22]</sup> By preventing the direct contact between methane and air, a highly concentrated product stream can be collected which eliminates the energy-intensive penalty for downstream gaseous product purification. The nature of lattice oxygen mediated chemical looping technology is redox reactions involving methane molecules absorption and C–H bond dissociation on metal-oxide based oxygen carrier surfaces, lattice oxygen ion diffusion, oxygen vacancy creation and annihilation at high temperatures.<sup>[23,24]</sup> The state-of-the-art process design has achieved an overall chemical looping operation over 3000 cycles.<sup>[25]</sup> One key challenge in chemical looping process is to improve the catalytic reactivity of oxygen carrier in activating the C–H bond significantly. Tremendous efforts have been devoted to design and development of commercially viable oxygen carriers in chemical looping systems,<sup>[16,26–32]</sup> yet the occurrence of carbon deposition still challenges the use of highly active material for oxygen carriers. Thus, an optimal oxygen carrier material design that possesses both high catalytic reactivity and carbon resistance is of great interest and significance.

Herein this work we develop a hybrid oxygen carrier design strategy based on perovskite-hematite materials to exemplify the concept to preventing carbon deposition while converting alkanes with low energy consumption, environmental impact or capital cost. Perovskite  $\text{LaFeO}_3$  (LFO) is a promising materials exhibiting high catalytic activity for CLPO of methane to syngas due to its high ionic conductivity and low activation energy barriers in C–H bond dissociation,<sup>[33–37]</sup> yet the syngas yield is substantially affected by inevitable carbon deposition in long term operation. Additionally, non-reversible structural change can also occur in perovskites<sup>[38]</sup> due to their low oxygen carrying capacity. On the other hand, hematite  $\text{Fe}_2\text{O}_3$  (FO) has long been considered as a promising material for commercialized oxygen

carrier due to its high oxygen carrying capacity, stable structure, low cost, and low environmental impact. Nevertheless, the reactivity of FO to methane is low to moderate at temperatures below 900 °C.<sup>[19,39,40]</sup> In this work we develop a hybrid LFO-FO material that fuses the advantages of LFO and FO together by utilizing a low concentration of LFO as the active component and a high concentration of FO as a dynamic oxygen reservoir. Atomistic level understanding of  $\text{CH}_4$  activation and carbon dissipation/deposition on LFO obtained from density functional theory (DFT) calculations guides the design concept of hybrid LFO-FO oxygen carriers. The experimental results demonstrate the hybrid LFO-FO is not only highly selective to syngas production, but also exhibits excellent carbon inhibition capability even at high temperatures. The concept of hybrid material is expected to be a promising strategy for designing active materials with resilient carbon resistance in alkane conversion systems.

## Computational and Experimental Section

### Density functional theory (DFT) calculations

*Ab initio* density functional theory calculations were carried out using the Vienna *Ab initio* simulation package (VASP), which adopts the projector augmented wave (PAW) pseudopotentials to describe the electron-core interaction.<sup>[41–44]</sup> The generalized gradient approximation (GGA) of Perdew, Burke, and Ernzerhof (PBE) was used to account for electron exchange correlation effects.<sup>[45]</sup> Spin-polarized DFT+*U* formalism of Dudarev et al. was employed to address the on-site Coulomb interactions between the localized Fe 3*d*-electrons,<sup>[46,47]</sup> and the chosen effective *U* value for LFO and FO were 4.64 eV and 4.0 eV,<sup>[48,49]</sup> respectively. The LFO material considered in this work is in an orthorhombic perovskite structure (*Pnma* 62) with the G-type anti-ferromagnetism as shown in

Figure 2a,<sup>[50]</sup> and the FO has a hexagonal corundum structure ( $R\bar{3}C$ ) with its ground state adopting an antiferromagnetic ordering along the hexagonal (0001) axis as presented in Figure 2b.<sup>[51]</sup> Using a kinetic energy cutoff of 600 eV, the Brillouin zone of the LFO and FO were respectively sampled by a  $6 \times 4 \times 6$  and a  $6 \times 6 \times 4$  Monkhorst-Pack  $k$ -point grids,<sup>[52]</sup> and the full relaxation of the bulk structures were carried out until the residual forces were less than 1 meV/Å. The calculated lattice parameters for LFO ( $a = 5.57$  Å  $b = 7.90$  Å and  $c = 5.63$  Å) and FO ( $a = b = 5.07$  Å and  $c = 13.88$  Å) are both in good agreement with the experimental results in the literature.<sup>[53,54]</sup>

The LFO and FO surfaces were simulated by slab models that were cleaved from the optimized bulk structures. A vacuum layer of more than 16 Å was added to the surface models to avoid interactions between the slabs and their periodic replicates along the  $z$ -direction. For surface calculations, a kinetic energy cutoff of 400 eV and a  $2 \times 2 \times 1$  Monkhorst-Pack  $k$ -point mesh was used until the residual forces were less than 0.02 eV/Å. Furthermore, the long-range dispersion interactions between CH<sub>4</sub> and the surface was considered using the DFT-D3 method of Grimme.<sup>[55,56]</sup> The strength of the interaction between the studied molecule and the surface was evaluated by the adsorption energy ( $E_{\text{adsorbate,ad}}$ ):

$$E_{\text{adsorbate,ad}} = E_{\text{sys}} - (E_{\text{slab}} + E_{\text{adsorbate,free}}) \quad (1)$$

where  $E_{\text{sys}}$  is the total energy of the system with an adsorbed molecule;  $E_{\text{slab}}$  is the energy of the surface; and  $E_{\text{adsorbate,free}}$  is the energy of an isolated adsorbed molecule in vacuum. Based on this definition, a more negative value of  $E_{\text{adsorbate,ad}}$  represents a more exothermic and thermo-favorable process, and thus a more stable adsorption configuration. Transition states (TS) were located by the climbing-image nudged elastic band (CI-NEB) method.<sup>[57–60]</sup> Ionic charges were computed by the Bader method.<sup>[61,62]</sup>

### Sample preparation and performance

Perovskite LFO, hematite FO and hybrid LFO-FO with overall La/Fe ratio 0.2–5% were synthesized by modified Pechini synthesis (see supporting information S2). Approximately 15 mg powder samples were mounted in an alumina crucible, and continuous reduction-oxidation cycles were conducted using a Setaram SETSYS Evolution

Thermogravimetric Analyzer (TGA). The reduction step was performed using 25% CH<sub>4</sub> (50 mL/min) balanced by inert gas (50 mL/min of N<sub>2</sub> and 100 mL/min of He) for 5 minutes. The oxidation step was performed in 25% air (50 mL/min) balanced with inert gas for 5 minutes. A 10 min flushing step using the same flow rate of inert gas was adopted in between to prohibit the mixing of oxygen and CH<sub>4</sub>. When analyzing the TGA data, reduction conversion  $X_r$  is defined by the following equation:

$$X_r = \frac{w_i - w_t}{w_o} \times X_r 100 \% \quad (2)$$

where  $w_i$  is the initial weight (mg) of oxygen carriers in TGA;  $w_t$  is the weight of oxygen carriers after 5 min reduction of materials by 25% CH<sub>4</sub>; and  $w_o$  represents the weight of oxygen in initial oxygen carriers. The definition of oxidation conversion ( $X_o$ ) is shown as the following equation:

$$X_o = \frac{w_f - w_t}{w_o} \times 100 \% \quad (3)$$

where  $w_f$  is the final weight of oxygen carriers after oxidation regeneration.

Temperature programmed reduction reaction (TPR) was conducted in the same Setaram SETSYS Evolution TGA. 15 mg samples were mounted and heated from 500 °C to 1000 °C at a 10 °C/min temperature increment in 10% CH<sub>4</sub> (20 mL/min CH<sub>4</sub> balanced with 180 mL/min He). The composition of gas outlet was analyzed and recorded by a MKS mass spectrometer (MS).

All the samples were analyzed using a Rigaku SmartLab X-ray Diffractometer (XRD) with eliminated fluorescence. Scans were run from 20–80 degrees at a rate of 1 degree per minute with an accelerating voltage and filament current of 40 kV and 44 mA, respectively. All of the XRD spectra were analyzed using PDXL software and identified with the JCPDS database. Scanning electron microscope (SEM) images were taken with a 10 kV and 0.17 nA electron beam. Secondary electron images were obtained with a working distance of 4.1 mm. A Kratos Axis Ultra DLD spectrometer was used to obtain X-ray photoelectron (XPS) spectra. Mg K $\alpha$  monochromatic X-ray radiation (1253.8 eV) was applied to ensure

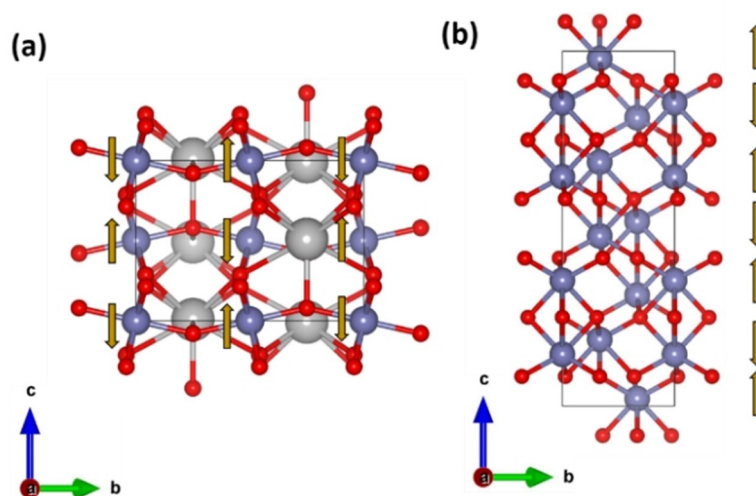


**Figure 2.** Bulk structures of the modeled LFO (a) and FO (b) materials. Fe, La, and O atoms are depicted in purple, grey, and red, respectively. Yellow arrows indicate the up and down spin states of the Fe atoms for the corresponding anti-ferromagnetism.

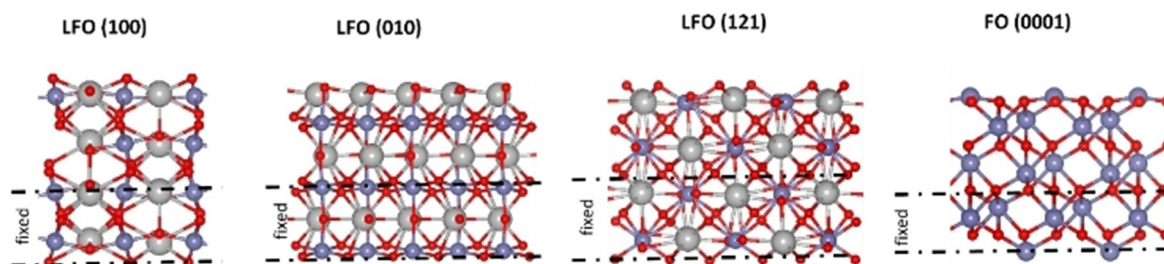


Figure 3. Configurations of the optimized LFO and FO surface models.

the optimal peak intensity of Cu. The spectra were collected at room temperature. Binding energy (B.E.) values were referenced to the standard C 1s binding energy of 284.8 eV. The CasaXPS program was used for data analysis. Shirley-type background and Lorentzian-Gaussian combination were used for data processing.

## 2. Results and Discussion

LFO has been widely reported to be a reactive material in activating methane in the literature, yet a detailed mechanism study of the C–H bond cleavage of methane on LFO is limited. Hence, *Ab initio* DFT calculations were performed to gain an insight into the excellent reactivity of LFO in initiating CH<sub>4</sub> dissociation. The most thermodynamically favorable LFO surfaces were examined in this work, including the LFO (121), (100), (010). The LFO (121) and (100) planes are theoretically the most stable surfaces of LFO and confirmed by XRD analysis and high-resolution transmission electron microscopy (HRTEM) observation in the literature.<sup>[63–65]</sup> LFO (010), despite its relatively low thermodynamic stability, still possesses a significant population in the equilibrium morphology.<sup>[48,63]</sup> In addition, the (010) surface has been reported to be the active surface for other perovskite families,<sup>[66]</sup> thus it is considered in this work. The catalytic activity of all LFO (121), (100), and (010) planes in cleaving the C–H bond of CH<sub>4</sub> were investigated, and the results are compared with that of FO, one of the most promising material for CLPO of CH<sub>4</sub>. The optimized surface models are presented in Figure 3, where the most thermodynamically stable terminations of LFO reported by Blanck et al. were adopted,<sup>[63]</sup> and the Fe-terminated FO (0001) surface was selected because it is the most thermodynamically stable surface of FO under oxygen-lean chemical looping environment.<sup>[67–69]</sup> The LFO (121) and (010) and FO (0001) surfaces were modeled by periodic  $p(2 \times 2)$  slabs with 4 stoichiometric layers, and the LFO (100) plane was simulated using a periodic  $p(2 \times 1)$  slab with 3 stoichiometric layers.

A systematic exploration of the CH<sub>4</sub> adsorption site on the selected LFO and FO surfaces was performed, and the most stable CH<sub>4</sub> adsorption configurations are presented in Figure 4a with the corresponding adsorption energies summarized in Table 1. To understand the dominating CH<sub>4</sub> binding mechanism on the different surfaces,  $E_{\text{CH}_4, \text{ad}}$  is decomposed into  $E_{\text{CH}_4, \text{elec}}$  and  $E_{\text{CH}_4, \text{disp}}$ , which respectively accounts for the electronic and

Table 1. Adsorption energies (eV) of CH<sub>4</sub> on the studied surfaces, and the electrons ( $e^-$ ) gained by the CH<sub>4</sub> molecule after adsorption.

	LFO (010)	LFO (100)	LFO (121)	FO (0001)
$E_{\text{CH}_4, \text{ad}}$	−0.539	−0.240	−0.196	−0.295
$E_{\text{CH}_4, \text{elec}}$	−0.340	−0.052	−0.044	−0.110
$E_{\text{CH}_4, \text{disp}}$	−0.199	−0.189	−0.152	−0.185
$ q_{\text{CH}_4} $	0.054	0.005	0.005	0.024

dispersion interactions. Among all the studied surfaces, LFO (010) is not only identified to be the most active surface toward CH<sub>4</sub> since its  $E_{\text{CH}_4, \text{ad}}$  is significantly higher than the others (ca. > 0.2 eV), but it is also the only surface where the electronic interaction dominates the CH<sub>4</sub> binding mechanism (i.e.,  $E_{\text{CH}_4, \text{elec}} > E_{\text{CH}_4, \text{disp}}$ ). Furthermore, LFO (010) has the highest  $E_{\text{CH}_4, \text{elec}}$  value among the studied surfaces, which suggests it has the strongest electronic interactions with CH<sub>4</sub>. This is consistent with results obtained from the Bader charge analysis as listed in Table 1, where the amount of charge gained by the CH<sub>4</sub> molecule ( $|q_{\text{CH}_4}|$ ) after adsorption are in the following order: LFO (010) > FO (0001) > LFO (121) and (100). Moreover,  $E_{\text{CH}_4, \text{ad}}$  was found to be linearly correlated to  $|q_{\text{CH}_4}|$  as illustrated in Figure 4b. To further explore the catalytic reactivity of the studied surfaces, the barrier of the initial C–H bond cleavage of CH<sub>4</sub> were investigated. Figure 4c illustrates the minimum energy pathway (MEP) for CH<sub>4</sub> dissociation on the different surfaces, which is a heterolytic step with the dissociated CH<sub>3</sub> and H respectively bind on the metal sites and the surface lattice oxygen sites, and the configurations of TSs and final states (FSs) are provided in Figure S1. The most facile C–H bond activation of CH<sub>4</sub> was found on the LFO (010) surface because of the lowest barrier it requires, which can be attributed to its strongest electronic interactions with CH<sub>4</sub> among all the surfaces. Owing to its highest adsorption energy and the lowest CH<sub>4</sub> activation barrier among the studied surfaces, LFO (010) is proposed to be the most favorable surface for the superior reactivity toward CH<sub>4</sub> conversion in LFO.

However, the highly reactive nature of LFO for CH<sub>4</sub> activation inevitably promotes the undesired carbon formation on its surface. Specifically, these carbon atoms are expected to either diffuse on the surface prior to interact with each other to form C–C compounds, or diffuse into the LFO lattice with the presence of oxygen vacancies in the sublayers of LFO.



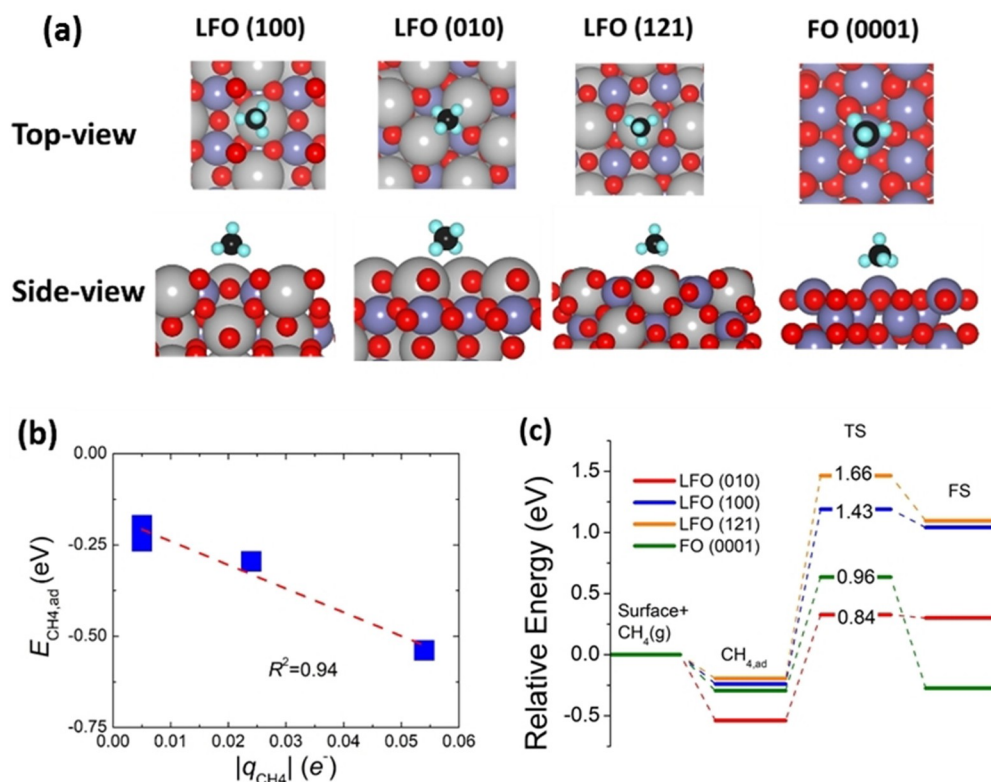


**Figure 4.** (a) The most stable CH<sub>4</sub> adsorption configurations, (b) the linear correlation between  $E_{\text{CH}_4, \text{elec}}$  and  $|q_{\text{CH}_4}|$ , and (c) the MEP of CH<sub>4</sub> activation on the studied surfaces. Value of barriers are labeled on the MEP.

Clusterization of the carbon atoms will lead to layered carbon deposition and deactivates the oxygen carriers. Unlike the conventional hydrocarbon steam reforming processes in which carbon is combusted by the oxidative gaseous feedstock, the removal of adsorbed carbon atoms is achieved through oxidation with the lattice oxygen provided by LFO in the reducing environment of the chemical looping methane conversion. Hence, a detailed understanding of the thermodynamics and kinetics of the elementary carbon evolution on LFO is crucial in providing a possible direction of material optimization. In this work we modeled and examined the competition between carbon deposition and dissipations over pristine and oxygen-deficient LFO (010). The related elementary steps of carbon atom on the pristine surface was first investigated, and the La-La bridge site was found to be the most stable adsorption site with  $E_{\text{C,pristine}} = -2.44$  eV. The corresponding energy profile of oxidation, diffusion, and the C–C coupling of the adsorbed carbon atoms were also calculated and presented in Figure 5. The barrier of carbon oxidation (0.26 eV) is much lower than the surface diffusion (0.43 eV) and C–C coupling (0.85 eV), which indicates the carbon removal on the pristine surface is efficient with sufficient lattice oxygen supplies.

Lattice oxygen is extracted from LFO in the oxidation with methane and the related intermediates. Consequently, oxygen-deficient LFO (010) surfaces play an important role in the reducing state of the CLPO process. In order to identify the

thermodynamically preferred defective structures, the formation energy of oxygen vacancies ( $O_{\text{vc}}$ ),  $E_{O_{\text{vc}}}$ , was calculated by the following equation:

$$E_{O_{\text{vc}}} = E_{\text{defective}, N} + \frac{N}{2} E_{O_2} - E_{\text{perfect}} \quad (4)$$

where  $N$  is the number of  $O_{\text{vc}}$ ;  $E_{\text{defective}, N}$  and  $E_{\text{perfect}}$  are the energies of the defective surface with  $N$   $O_{\text{vc}}$  and the pristine surface, respectively; and  $E_{O_2}$  is the energy of a triplet  $O_2$  molecule in gas phase. Following such a definition, a more positive  $E_{O_{\text{vc}}}$  indicates a higher energy input is required for  $O_{\text{vc}}$  formation, and hence a less stable configuration. The calculated  $E_{O_{\text{vc}}}$  of the 1<sup>st</sup>, the 2<sup>nd</sup>, and the 3<sup>rd</sup> topmost layers of LFO (010) are 3.72 eV, 3.55 eV, and 3.84 eV, respectively, which reveals that the  $O_{\text{vc}}$  formation is thermodynamically preferable in the second layer. Furthermore, the oxygen anion diffusion from the second atomic layer to the topmost surface was found to be facile with only a 0.04 eV barrier as illustrated in Figure S2. As a result, the surface lattice oxygen on the stoichiometric LFO (010) plane can be replenished efficiently by the sublayer lattice oxygen in the initial stage of CLPO, hence maintaining a high carbon removal rate.

Despite the efficient oxygen anion replenishment of LFO (010), a higher extent of lattice oxygen dissipation can ultimately lead to the expansion of oxygen-deficient surfaces. For the 1- $O_{\text{vc}}$  surfaces, carbons are found to bind preferentially

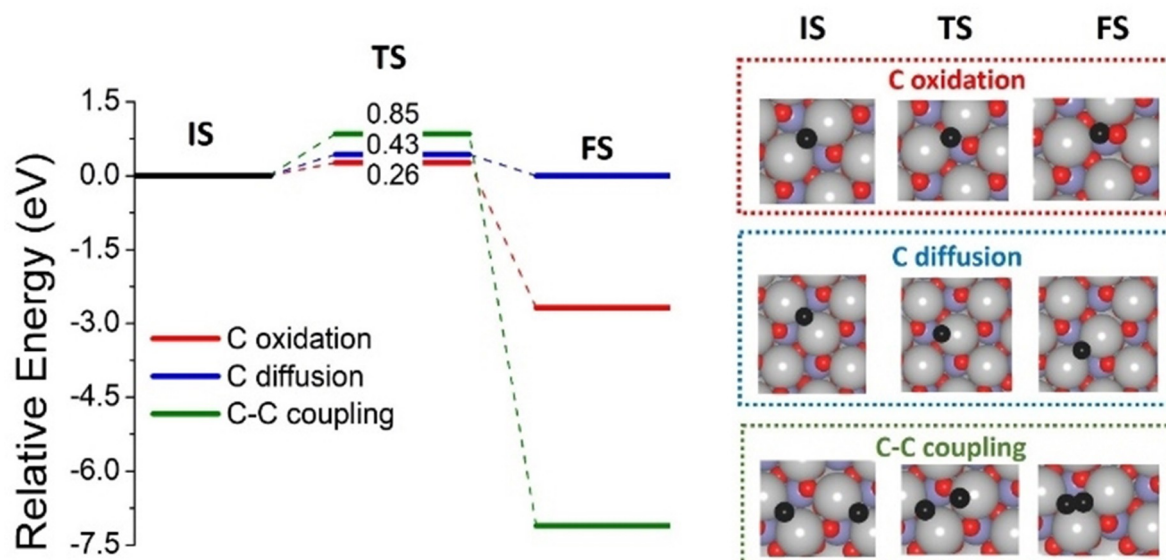


**Figure 5.** MEP and the top view of the initial states (IS), transition states (TS) and final states (FS) of carbon oxidation, diffusion, and coupling on the pristine LFO (010) surface. Value of barriers (eV) are labelled on the MEP.

at the  $O_{VC}$  sites as illustrated in Figure 6a, and the carbon chemisorption energies ( $-3.86$  and  $-4.22$  eV when the  $O_{VC}$  is in the 1<sup>st</sup> layer and the 2<sup>nd</sup> layer, respectively) are dramatically higher than that on the pristine surface ( $-2.44$  eV). Furthermore, the higher carbon binding energy on the defective surfaces results in the much higher carbon oxidation barriers ( $0.59$  and  $0.67$  eV when the  $O_{VC}$  is in the 1<sup>st</sup> layer and the 2<sup>nd</sup> layer, respectively) than the pristine surface ( $0.26$  eV) as indicated in the MEP of Figure 6a, which substantially slows down the carbon removal rate. Figure 6b provides the reaction pathway of C–C couplings on the 1- $O_{VC}$  surfaces, and the results reveal that C–C couplings becomes extremely facile due to their nearly zero barriers (both are  $0.04$  eV), which promotes the formation of undesired carbon clusterization on the surface.

In short, the fast kinetics of carbon removal and high barrier of C–C coupling on the pristine LFO surface are the desired properties for carbon inhibition. However, the excellent catalytic reactivity of LFO towards  $CH_4$  makes it vulnerable to carbon deposition, because more  $O_{VC}$  were created on the surface as the reaction progresses, which results in a stronger carbon binding that significantly reduce the kinetics of carbon removal through oxidation with lattice oxygen. Furthermore, the unremoved carbon would act as a seed for the C–C coupling which is significantly promoted by the presence of  $O_{VC}$ , and triggers the cascade of the subsequent carbon clusters formation. As a result, maintaining sufficient lattice oxygen on surface is key in maximizing the carbon resistance of LFO. By exploiting the fact that the active LFO (010) prefers sublayer  $O_{VC}$  formations and its surface oxygen replenishment is facile, it is speculated the number of surface  $O_{VC}$  can be mitigated if sufficient lattice oxygen is provided during the reaction, thereby preventing the cascade of carbon deposition.

Enlightened by the theoretical DFT prediction, a hybrid LFO-FO material is designed in which methane is converted by the

active LFO while FO serves as an oxygen reservoir that replenishes the lattice oxygen of the reactive LFO surfaces and thereby suppresses carbon deposition. The coking will be triggered substantially once the amount of lattice oxygen is not sufficient to support effective oxygen transport in the FO oxygen reservoir, especially at high temperatures. Hence the oxygen reservoir is replenished in the cyclic regeneration reactions. Varying LFO concentration (0.2% to 5%) in hybrid LFO-FO was investigated in order to optimize the particle reactivity. Phase analysis (Figure. S3) reveals that a low concentration of 0.2% LFO has no significant reactivity enhancement on LFO-FO, implying no effective hybrid structure formation occurs at LFO concentration 0.2% or lower. A higher LFO concentration of 2% or 5% result in minimal carbon inhibition capability in CLPO of methane (Figure S4 and S5). Thus, the excellent carbon resistance in the hybrid LFO-FO material is a synergistic effect between LFO and FO. 0.5% LFO with 99.5% FO demonstrates the highest reactivity and best carbon inhibition capability, thus the ratio of LFO to FO is adopted in the sample LFO-FO.

The impact of cyclic redox reaction on morphology and crystal phase has been conducted in hybrid LFO-FO. The high temperature treatment in sample preparation results in the thermal dynamically most stable surfaces. The XRD patterns before and after redox cycles are shown in Figure 7a and 7b. All the peaks labelled with asterisk can be identified to perovskite  $LaFeO_3$  while unlabeled peaks can be identified to rhombohedral  $Fe_2O_3$ . No other impurity phase was observed in the reacted sample, indicating the hybrid oxygen carrier has high phase stability during redox reactions. SEM images in Figure 7c and 7d prove that the hybrid LFO-FO has minimal morphological variation after cyclic reactions, which is beneficial to CLPO due to high structural stability. The LFO crystals, with a size of 500–

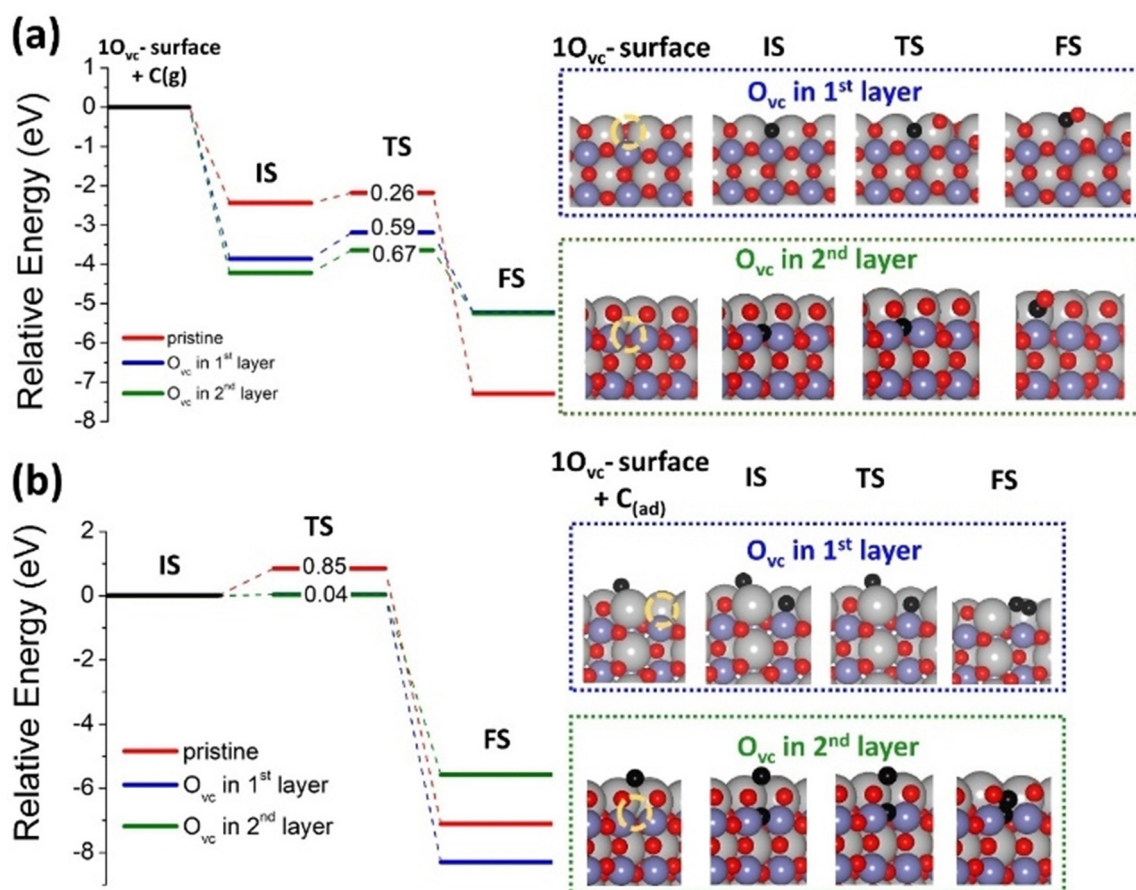


**Figure 6.** MEP and the side view of the initial states (IS), transition states (TS) and final states (FS) on LFO(010) surfaces (a) the 1- $O_{vc}$  surface with carbon adsorption and carbon oxidation; (b) the 1- $O_{vc}$  surfaces with the carbon adsorption and the C–C coupling. Dotted yellow circles indicate oxygen vacancies. Value of barriers (eV) are labeled on the MEP, and the results of pristine surfaces are also attached for comparison.

700 nm, are well dispersed and located on the grain boundaries of FO, as identified by SEM and EDS mapping.

Figure 8 displays the TPR profiles of hybrid LFO-FO oxygen carrier. LFO and FO oxygen carriers were also tested as comparisons. The unit of %/g<sub>o</sub> was adopted to eliminate possible influence by different sample weight on gas concentrations and better compare the performance of FO, LFO and LFO-FO. The gas concentration is normalized by the weight of total available oxygen in the sample, as shown below.

The unit of Y-axis (%/g<sub>o</sub>) was adopted to eliminate possible influence by different sample weight on gas concentrations and better compare the performance of FO and LFO-FO. The gas concentration is normalized by the weight of total available oxygen in the sample, as shown below.

$$\text{Concentration} = \frac{x_i}{m_{Fe_2O_3}} \times 30\% \quad (5)$$

where  $x_i$  stands for gas mole fraction,  $m_{Fe_2O_3}$  is the weight of  $Fe_2O_3$  in the total sample, and 30% is the weight percentage of oxygen in  $Fe_2O_3$ . The hybrid LFO-FO oxygen carrier exhibits excellent carbon inhibition capability between 500 °C and 1000 °C. At a reaction temperature of 950 °C, the gas product of

CLPO with the hybrid LFO-FO oxygen carrier is 13%/g<sub>o</sub> CO<sub>2</sub>, 700%/g<sub>o</sub> CO and 1400%/g<sub>o</sub> H<sub>2</sub>, respectively. This indicates that hybrid LFO-FO can achieve a high syngas selectivity over 98% which is the highest selectivity in bulk oxygen carrier design so far. The H<sub>2</sub>:CO ratio of 2:1 confirms that all the CH<sub>4</sub> was converted to syngas with no element carbon formation. By comparison, the reactivity of FO oxygen carrier remains low in the tested operating temperature window. At 1000 °C the CO selectivity is only 90% with product concentrations of CO<sub>2</sub>, CO and H<sub>2</sub> 5%/g<sub>o</sub>, 50%/g<sub>o</sub> and 100%/g<sub>o</sub>, respectively. On the other hand, LFO exhibits high reactivity with CH<sub>4</sub>, the peak at 624 °C suggests a H<sub>2</sub>:CO of 2:1 and a much lower onset reaction temperature than hybrid LFO-FO. However, A H<sub>2</sub>:CO ratio significantly higher than 2:1 indicates severe carbon deposition occurring at as low as 630 °C, also marked with dotted boxes in Figure 8(a), (c) and (d), suggesting a narrow operating temperature window in LFO and its strong tendency towards carbon deposition. In addition, a moderate CO selectivity of 94% is achieved in LFO, with the gas products detected at 624 °C are 3%/g<sub>o</sub> CO<sub>2</sub>, 50%/g<sub>o</sub> CO and 100%/g<sub>o</sub> H<sub>2</sub>, respectively. Nevertheless, the narrow temperature operating window of LFO cannot meet the requirement of CLPO temperature swing of 100 °C from inlet to outlet in a reducer.



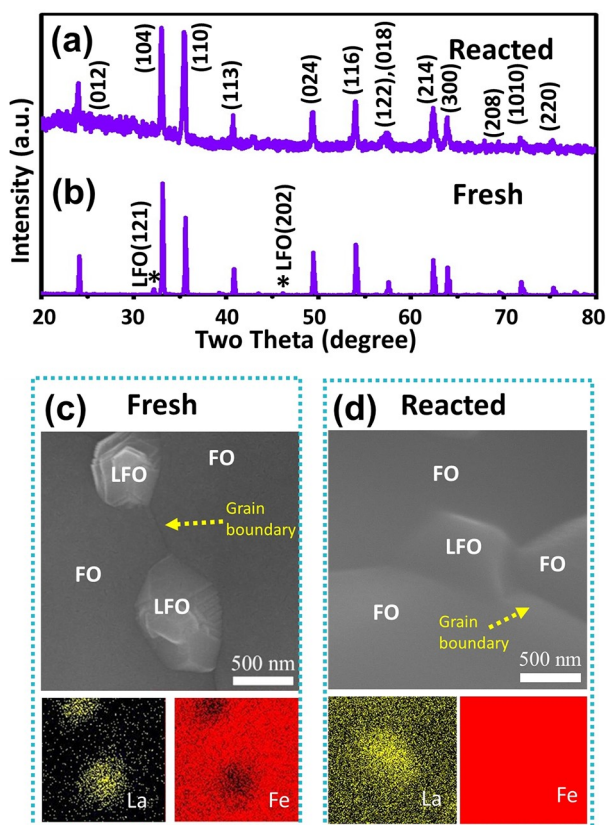


**Figure 7.** XRD of FO, hybrid LFO-FO, and LFO samples (a) before and (b) after 60 redox reaction cycles. SEM image of hybrid LFO-FO with EDS mapping images (c) before and (d) after redox reactions.

The TGA analysis was applied for multiple redox cycles to study the recyclability and conversion rates of the hybrid LFO-FO oxygen carrier. A longer reaction time is allowed to mimic moving bed reducer. Figure 9 shows oxygen carrier conversion rates in 10 continuous methane conversion cycles. The conversion rate of hybrid LFO-FO oxygen carriers is 275%, 359%, 349%, and 17.9% higher compared with pure FO oxygen carriers at 600 °C, 700 °C, 800 °C, and 900 °C, respectively.

### 3. Conclusions

Carbon deposition occurs inevitably on oxygen-deficient surfaces in hydrocarbon conversions, and the tendency of carbon atoms clusterization becomes higher with increased oxygen vacancies as cascade reactions. Guided by atomistic modelling which suggests hybrid oxygen carrier is capable of inhibiting the cascade reactions in carbon deposition, we have demonstrated that hybrid LFO-FO oxygen carrier with 0.5% LFO exhibits excellent reactivity, recyclability and carbon inhibition capability in chemical looping partial oxidation of methane between 500 and 1000 °C. In the hybrid oxygen carrier, the syngas selectivity is over 98% and the yield is 13 times higher than that in perovskite LFO or hematite FO oxygen carriers. There are two key factors in a hybrid oxygen carrier, one is that the LFO provides active site for methane conversion while the FO is a lattice oxygen reservoir that replenishes oxygen anions in reducing environment. Carbon deposition in a hybrid oxygen carrier can only be suppressed with high concentration of FO which supplies abundant lattice oxygen to LFO. High concentration of LFO will cause over-extraction of lattice oxygen from oxygen reservoir. This work opens up a path to a design

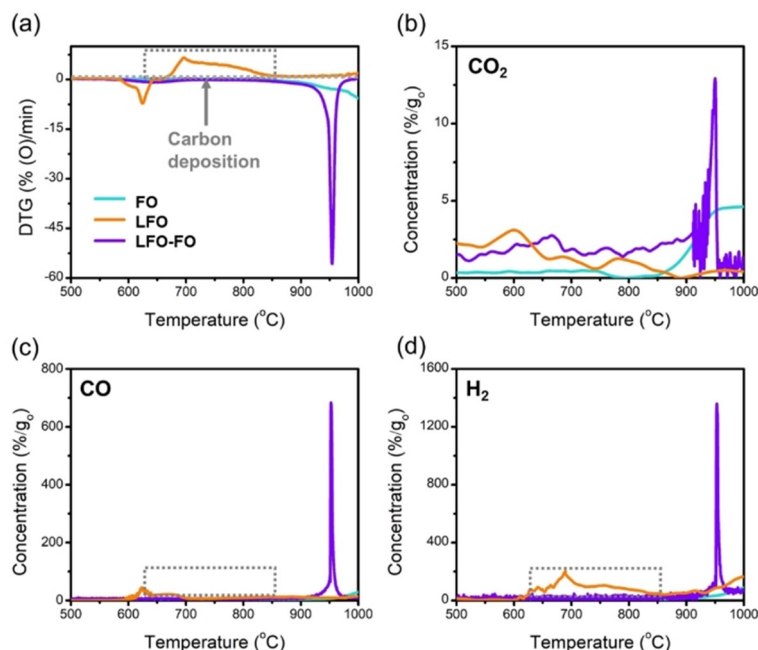


**Figure 8.** Temperature programmed reduction (TPR) profiles of FO, LFO, and LFO-FO. (a) Derivative thermo-gravimetric (DTG), (b) CO<sub>2</sub> concentration, (c) CO concentration, and (d) H<sub>2</sub> concentration.



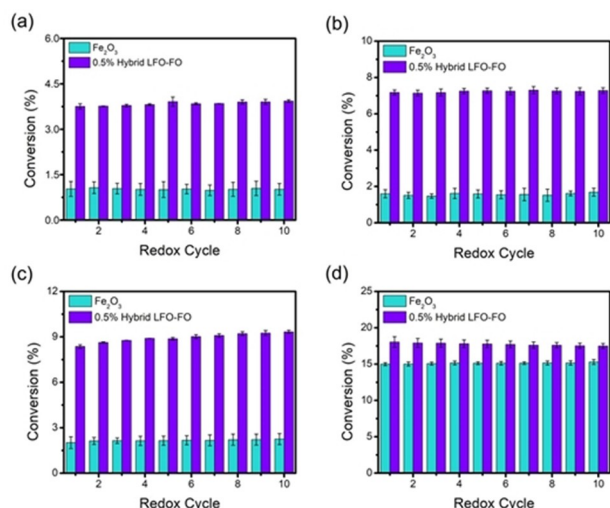


**Figure 9.** Cyclic oxygen carrier reduction conversion rate results of FO, hybrid LFO-FO at (a) 600 °C, (b) 700 °C, (c) 800 °C, and (d) 900 °C with 25 % CH<sub>4</sub> balanced by inert gas.

strategy with hybrid structured oxygen carriers for viable commercialization of chemical looping technology. It will not only renovate the chemical looping partial oxidation process, but also benefit other redox involved reactions such as photo-catalysis and chemical looping combustion.

## Acknowledgements

The service support provided by the Center for Electron Microscopy and the Analysis and NanoSystem Laboratory at The Ohio State University and the computing support provided by the Ohio Supercomputer Center are gratefully acknowledged.

## Conflict of Interest

The authors declare no conflict of interest.

**Keywords:** chemical looping partial oxidation • coking-resistant • hybrid oxygen carrier • density functional theory

- [1] J. A. Labinger, J. E. Bercaw, *Nature* **2002**, 417, 507–514.
- [2] BP, BP Energy Outlook 2016 Edition. (BP, London, UK, 2016).
- [3] IEA, *Energy and Air Pollution*. (International Energy Agency, 2016).
- [4] A. P. York, X. Xiao, M. L. Green, *Top. Catal.* **2003**, 22, 345–358.
- [5] D. J. Wilhelm, D. R. Simbeck, A. D. Karp, R. L. Dickenson, *Fuel Process. Technol.* **2001**, 71, 139–148.
- [6] B. Christian Enger, R. Lødeng, A. Holmen, *Appl. Catal. A* **2008**, 346, 1–27.
- [7] L. Bobrova, N. Vernikovskaya, V. Sadykov, *Catal. Today* **2009**, 144, 185–200.
- [8] M. E. Dry, *Catal. Today* **2002**, 71, 227–241.
- [9] A. Y. Khodakov, W. Chu, P. Fongarland, *Chem. Rev.* **2007**, 107, 1692–1744.
- [10] A. P. E. York, T. Xiao, M. L. H. Green, *Top. Catal.* **2003**, 22, 345–358.
- [11] J. Rostrup-Nielsen, *Catal. Sci. Technol.* **1984**, 5, 1–117.
- [12] S. S. Bharadwaj, L. D. Schmidt, *Fuel Process. Technol.* **1995**, 42, 109–127.

- [13] L. Zeng, Z. Cheng, J. A. Fan, L.-S. Fan, J. Gong, *Nat. Chem. Rev.* **2018**, 2, 349–364.
- [14] L.-S. Fan, F. Li, *Industrial and Eng. Chem. Res.* **2010**, 49, 10200–10211.
- [15] L. Zeng, S. Luo, F. Li, L.-S. Fan, *Zhongguo Kexue: Huaxue* **2012**, 42, 260–281.
- [16] M. Anheden, G. Svedberg, *Sci. J.* **1998**, 39, 1967–1980.
- [17] A. Lyngfelt, *Appl. Energy* **2014**, 113, 1869–1873.
- [18] M. V. Kathe, A. Empfield, J. Na, E. Blair, L.-S. Fan, *Appl. Energy* **2016**, 165, 183–201.
- [19] S. Luo, L. Zeng, D. Xu, M. Kathe, E. Chung, N. Deshpande, L. Qin, A. Majumder, T. Hsieh, A. Tong, Z. Sun, L.-S. Fan, *Energy Environ. Sci.* **2014**, 7, 4104–4117.
- [20] M. Kathe, A. Empfield, P. Sandvik, C. Fryer, Y. Zhang, E. Blair, L.-S. Fan, *Energy Environ. Sci.* **2017**, 10, 1345–1349.
- [21] L. Qin, Z. Cheng, M. Guo, M. Xu, J. A. Fan, L.-S. Fan, *ACS Energy Lett.* **2017**, 2, 70–74.
- [22] A. Tong, D. Sridhar, Z. Sun, H. R. Kim, L. Zeng, F. Wang, D. Wang, M. V. Kathe, S. Luo, Y. Sun, L.-S. Fan, *Fuel* **2013**, 103, 495–505.
- [23] A. Tong, S. Bayham, M. V. Kathe, L. Zeng, S. Luo, L.-S. Fan, *Appl. Energy* **2014**, 113, 1836–1845.
- [24] L. Qin, M. Guo, Z. Cheng, M. Xu, Y. Liu, D. Xu, J. A. Fan, L.-S. Fan, *J. Mater. Chem. A* **2017**, 5, 20153–20160.
- [25] C. Chung, L. Qin, V. Shah, L.-S. Fan, *Energy Environ. Sci.* **2017**, 10, 2318–2323.
- [26] K. Otsuka, Y. Wang, E. Sunada, I. Yamanaka, *J. Catal.* **1998**, 175, 152–160.
- [27] K. Li, H. Wang, Y. Wei, D. Yan, *Appl. Catal. B* **2010**, 97, 361–372.
- [28] X. Zhu, K. Li, Y. Wei, H. Wang, L. Sun, *Energy Fuels* **2014**, 28, 754–760.
- [29] S. Bhavsar, G. Vesper, *RSC Adv.* **2014**, 4, 47254–47267.
- [30] A. Kang, H. S. Lim, M. Lee, J. W. Lee, *Appl. Energy* **2018**, 211, 174–186.
- [31] Y. Du, X. Zhu, H. Wang, Y. Wei, K. Li, *Trans. Nonferrous Met. Soc. China* **2015**, 25, 1248–1253.
- [32] F. He, Y. Wei, H. Li, H. Wang, *Energy Fuels* **2009**, 23, 2095–2102.
- [33] S. Royer, D. Duprez, F. Can, X. Courtois, C. Batiot-Dupeyrat, S. Laassiri, H. Alamdari, *Chem. Rev.* **2014**, 114, 10292–10368.
- [34] F. He, J. Trainham, G. Parsons, J. S. Newman, F. Li, *Energy Environ. Sci.* **2014**, 7, 2033–2042.
- [35] L. Neal, A. Shafieifarhood, F. Li, *Appl. Energy* **2015**, 157, 391–398.
- [36] F. He, K. Zhao, Z. Huang, X. Li, G. Wei, H. Li, *Chin. J. Catal.* **2013**, 34, 1242–1249.
- [37] X. P. Dai, R. J. Li, C. C. Yu, Z. P. Hao, *J. Phys. Chem. B* **2006**, 110, 22525–22531.
- [38] A. Ksepko, *Int. J. Hydrogen Eng.* **2018**, 17, 9622–9634.
- [39] L. Qin, M. Guo, Z. Cheng, M. Xu, Y. Liu, D. Xu, J. A. Fan, L.-S. Fan, *J. Mater. Chem. A* **2017**, 5, 20153–20160.
- [40] L. Qin, M. Guo, Y. Liu, Z. Cheng, J. A. Fan, L.-S. Fan, *Appl. Catal. B*, 143–149.
- [41] G. Kresse, J. Hafner, *Inition Method. Phys. Rev. B* **1992**, 47, 558–561.
- [42] G. Kresse, J. Furthmüller, *J. Comput. Mater. Sci.* **1996**, 6 (1), 15–50.
- [43] C. Joubert, *Phys. Rev. B* **1999**, 59, 1758–1775.
- [44] P. E. Blöchl, *Phys. Rev. B* **1994**, 50, 17953–17979.
- [45] J. P. Perdew, K. Burke, M. Ernzerhof, *Phys. Rev. Lett.* **1996**, 77, 3865–3868.
- [46] S. Dudarev, G. Botton, *Phys. Rev. B* **1998**, 57, 1505–1509.
- [47] O. Bengone, M. Alouani, P. Blöchl, J. Hugel, *Phys. Rev. B* **2000**, 62, 16392–16401.
- [48] I. W. Boateng, R. Tia, E. Adei, N. Y. Dzade, C. R. A. Catlow, N. H. DeLeeuw, *Phys. Chem. Phys.* **2017**, 19, 7399–7409.
- [49] N. J. Mosey, P. Liao, E. A. Carter, *J. Chem. Phys.* **2008**, 129, 014103.
- [50] T. Arima, Y. Tokura, J. B. Torrance, *Var. Phys. Rev. B* **1993**, 48, 17006–17009.
- [51] F. Rollmann, A. Rohrbach, P. Entel, J. Hafner, *Phys. Rev. B* **2004**, 69, 165107.
- [52] J. Monkhorst, J. D. Pack, *Phys. Rev. B* **1976**, 13, 5188–5192.
- [53] S. E. Dann, D. B. Currie, M. T. Weller, M. F. Thomas, A. D. Al-Rawwas, *J. Solid State Chem.* **1994**, 109, 134–144.
- [54] L. W. Finger, R. M. Hazen, *J. Appl. Phys.* **1980**, 51, 5362–5367.
- [55] S. Grimme, J. Antony, S. Ehrlich, H. A. Krieg, *J. Chem. Phys.* **2010**, 132, 154104.
- [56] S. Grimme, S. Ehrlich, L. Goerigk, *J. Comput. Chem.* **2011**, 32, 1456–1465.
- [57] A. Henkelman, B. P. Uberuaga, H. Jónsson, *J. Chem. Phys.* **2000**, 113, 9901–9904.
- [58] G. Henkelman, H. Jónsson, *J. Chem. Phys.* **2000**, 113, 9978–9985.
- [59] D. Sheppard, R. Terrell, G. Henkelman, *J. Chem. Phys.*, **2008**, 128, 134106.
- [60] Vasp TST Tools, <https://theory.cm.utexas.edu/vtsttools>, (accessed April 16, 2020).

- [61] R. F. W. Bader, *Atoms in Molecules: A Quantum Theory*, Oxford University Press: New York, USA, 1994.
- [62] W. Tang, E. Sanville, G. A. Henkelman, *J. Phys. Condens. Matter* **2009**, *21* (8), 084204.
- [63] D. Blanck, E. Berrier, J. F. Paul, *ChemCatChem* **2017**, *9*.
- [64] I. Zhao, Y. Liu, X. Li, G. Lu, L. You, X. Liang, F. Liu, T. Zhang, Y. Du, *Sens. Actuators B* **2013**, *181*, 802–809.
- [65] Z. Li, L. Lv, J. Wang, X. Ao, Y. Ruan, D. Zha, G. Hong, Q. Wu, Y. Lan, C. Wang, *Nano Energy* **2018**, *47*, 199–209.
- [66] C.-W. Lee, R. K. Behera, E. D. Wachsman, S. R. Phillpot, S. B. Sinnott, *Phys. Rev. B*, 115418.
- [67] X. G. Wang, W. Weiss, Sh. K. Shaikhutdinov, M. Ritter, M. Petersen, F. Wagner, R. Schloegl, M. Scheffler, *Phys. Rev. Lett.* **1998**, *81*, 1038–1041.
- [68] R. J. Lad, V. E. Henrich, *Surf. Sci.* **1988**, *193*, 81–93.
- [69] M. Lübke, W. Moritz, *J. Phys. Condens. Matter* **2009**, *21*, 134010.

---

Manuscript received: July 20, 2020  
Revised manuscript received: October 6, 2020  
Accepted manuscript online: October 8, 2020  
Version of record online: November 6, 2020